applied sciences

MDPI

Article

Optimized Detection Algorithm for Vertical Irregularities in Vertical Curve Segments

Rong Xie [1] and Chunjun Chen [1,2,*]

[1] School of Mechanical Engineering, Southwest Jiaotong University, Chengdu 610031, China; xr0618@my.swjtu.edu.cn
[2] Technology and Equipment of Rail Transit Operation and Maintenance Key Laboratory of Sichuan Province, Chengdu 610031, China
* Correspondence: cjchen@swjtu.edu.cn

Abstract: The vertical curve is designed to smooth sudden gradient changes in the longitudinal profile, enhancing train operational safety and passenger comfort. However, dynamic detection in these segments has consistently encountered issues with long-wavelength vertical irregularities exceeding tolerance limits. To investigate the root causes of this phenomenon and develop a targeted solution, a comprehensive vehicle-track dynamics simulation model was first constructed, based on the design principles for intercity railway vertical curves. The inertial reference method was then applied to process the acceleration and relative displacement data between the detection beam and the track, yielding virtual irregularities. These were compared with excitation irregularities to identify key factors affecting detection accuracy in vertical curve segments. Through further analysis of abnormal exceedances in detection data, the reference cancellation method was proposed. By employing smoothing filters and orthogonal least squares fitting, this method effectively removes track alignment components from the acceleration integration results. Detection errors under various conditions were then compared between the two methods to evaluate the feasibility and effectiveness of the reference cancellation approach. Results indicate that regions with increased longitudinal profile detection errors are primarily located at and near gradient transition points. The vertical curve radius was found to be the primary factor influencing the accuracy of long-wavelength irregularity detection. The proposed reference cancellation method effectively reduces detection errors in areas near gradient transition points to levels comparable to other track sections. Compared to the inertial reference method, the reference cancellation method reduces the maximum detection error by up to 71.77% and the root mean square error by up to 86.61%, effectively mitigating the abnormal exceedances associated with vertical curves.

Keywords: vertical curve; long-wavelength irregularities; track irregularity detection; inertial reference method; reference cancellation method

Citation: Xie, R.; Chen, C. Optimized Detection Algorithm for Vertical Irregularities in Vertical Curve Segments. *Appl. Sci.* **2024**, *14*, 10753. https://doi.org/10.3390/app142210753

Academic Editor: Diogo Ribeiro

Received: 29 October 2024
Revised: 15 November 2024
Accepted: 19 November 2024
Published: 20 November 2024

1. Introduction

With the continuous expansion of urban rail transit mileage and the significant increase in train speeds, the operational safety of locomotives and the comfort of passengers have garnered considerable attention [1]. Deviations between the geometric configuration of the track and design standards, referred to as track irregularities [2], have become a primary factor contributing to vibrations in railway vehicles and track structures [3]. The presence of track irregularities exacerbates wheel-rail wear, leads to the loosening of track structures, and diminishes both the safety and efficiency of train operations [4–7]. Therefore, the rapid and accurate detection of track irregularities is essential for enhancing track quality, ensuring train safety, and facilitating effective track maintenance operations [8].

Based on existing dynamic inspection results and relevant literature, it is evident that the wavelength of irregularities affecting train ride comfort increases with operating speed [9]. However, detecting long-wavelength irregularities near vertical curves in

the track's longitudinal profile often leads to significant detection errors and frequent exceedances in measurement data [10]. Therefore, it is crucial to conduct in-depth research on the anomalies in detection data for vertical curve segments in the longitudinal profile.

Previous studies have predominantly focused on the parameter settings for railway vertical curves and the analysis of vehicle dynamics, with some investigations exploring the relationship between vertical curve parameters and track dynamic irregularities. For instance, in [11], the authors analyzed the relationship between the maximum vertical vibration acceleration of a train and the vertical curve radius, gradient, and length of the intervening straight section from the perspective of dynamic responses as the train traverses a vertical curve. They also provided recommended values for vertical curve parameters in high-speed railways operating at 400 km/h. In [12], the authors conducted an in-depth analysis of wheel-rail dynamics, focusing on the track profile parameters and ride comfort. They identified that the primary vertical vibration frequency induced by vertical curves is associated with operating speed and gradient length, noting that a concise gradient length can lead to overlapping vibrations at the beginning and end of the vertical curve. In [13], the authors proposed design recommendations for the track profile parameters by comprehensively considering the dynamic responses of both the vehicle and track systems, determining the dynamic indicators sensitive to variation. In [14], using theoretical analysis, simulation, and data comparison, the authors studied the impact of vertical curve parameters on various dynamic performance metrics. They provided recommended values for vertical curve radii at 400 km/h, considering safety, comfort, and maintenance requirements. The authors of [15] provided recommended values for the minimum radius and length of high-speed railway vertical curves, considering both operational safety and passenger comfort. In [16], the authors conducted theoretical analyses and simulations to investigate the adaptability of existing high-speed railways operating at 250 km/h to increased operational speeds, optimizing related technical standards, including the minimum vertical curve radius. The authors of [17] referenced metro design specifications to calculate relevant technical requirements for metro lines operating at 140 km/h. Additionally, the authors of [18] analyzed measured data from the Shanghai Railway Bureau on the Hangzhou–Changsha Passenger Dedicated Line, revealing correlations between core vertical curve parameters, locomotive operating speeds, and long-wavelength irregularity exceedances in the time domain. In [19], the authors explored the relationship between longitudinal profile parameters and track irregularity detection through simulation, subsequently recommending lengths for incline segments of high-speed rail designs with a target speed of 300 km/h. Lastly, the authors of [20] utilized extensive dynamic inspection data to investigate the influence of vertical curve parameters on track dynamic irregularities and proposed optimization strategies for these parameters.

In summary, existing research often integrates track design and maintenance experiences through theoretical and empirical analyses, as well as simulation calculations, to adjust longitudinal profile parameters, thereby enhancing passenger comfort and improving track smoothness. However, research focused on improving the detection accuracy of long-wavelength irregularities near vertical curves and preventing abnormal exceedances in inspection data remains insufficient, which is critical for informed decision-making in track maintenance operations.

The structure of the remainder of this paper is outlined as follows: In Section 2, a multibody dynamics model is established, focusing on the design principles for vertical curves and the inertial reference method, followed by validation of the constructed model. Section 3 investigates the relationships between key parameters—such as train speed, vertical curve radius, length, and gradient—and the detection accuracy of track irregularities, identifying the primary factors influencing detection accuracy. Section 4 analyzes the reasons for significant errors in detection data from vertical curve segments and introduces the reference cancellation method to mitigate the impact of the inertial reference (track alignment) on detection accuracy, with simulation experiments conducted to validate the proposed method's effectiveness. Finally, Section 5 presents the conclusions.

2. Virtual Track Inspection Technology

2.1. Multibody Dynamic Simulation Model

To investigate the relationship between dynamic detection accuracy of track vertical irregularities and variations in core parameters—such as train speed, vertical curve radius, length, and gradient—a comprehensive vehicle multibody dynamic model was developed using Simpack multibody dynamics simulation software, Simpack 2018.1-build66, 64 bit (as shown in Figure 1) to obtain virtual dynamic response signals. Subsequently, the virtual signals were processed using the inertial reference method, followed by digital high-pass filtering to obtain the track vertical irregularities, referred to in this study as "virtual vertical irregularities". Based on observed anomalies in dynamic inspection and the practical research requirements for long-wavelength irregularities, the spatial cutoff frequency of the filter was set to 120 m.

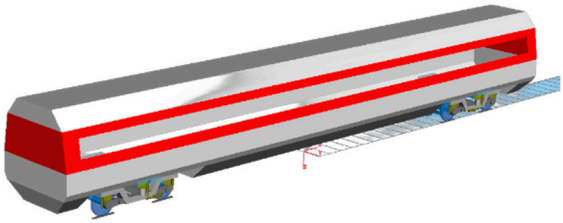

Figure 1. Comprehensive vehicle multibody dynamics model.

2.2. Vertical Curve

The vertical curve is a critical component in the longitudinal profile of railways, connecting segments with varying gradients to enhance operational safety and passenger comfort when trains pass through gradient transition points. In Simpack, the configuration of vertical curves is accomplished by inputting key parameters, including length and gradient. When the gradient difference between adjacent segments exceeds 1‰, a circular vertical curve is mandated to ensure smooth transitions, with the minimum radius governed by comfort criteria [21], The formula is as follows:

$$R_{\mathrm{sh}} \geq v^2/(3.6^2 a_{\mathrm{sh}}) \tag{1}$$

where R_{sh} is the radius of the vertical curve, v is the train speed, and a_{sh} is the allowable vertical centripetal acceleration based on passenger comfort criteria.

As metro systems and rapid transit lines with speeds exceeding 100 km/h continue to develop, various design codes and standards for track alignment have been established. However, discrepancies exist among technical standards and operational practises regarding values for vertical centripetal acceleration. For instance, the Metro Design Code (GB50157-2013) [22] stipulates two values—0.16 m/s^2 for standard conditions and 0.3 m/s^2 for challenging conditions—for lines operating at speeds below 100 km/h. In contrast, the Intercity Railway Design Code (TB 10624-2020) [23] and the Technical Specifications for Rapid Transit (T/CAMET 01001-2019) [24] define acceleration values for lines operating between 120 and 160 km/h, specifying limits of 0.15 m/s^2 and 0.26 m/s^2 for the former, and 0.25 m/s^2 and 0.34 m/s^2 for the latter, under standard and challenging conditions, respectively. Considering the additional margin introduced by rounding the vertical curve radius, this study standardizes the values of 0.15 m/s^2 for standard conditions and 0.3 m/s^2 for challenging conditions as the basis for further analysis and calculations.

2.3. Inertial Reference Method

Currently, the dynamic detection of track irregularities primarily relies on the inertial reference method [25]. This technique establishes a unified inertial reference using accelerometers, combined with distance sensors to capture the relative displacement between the detection system and the inertial reference, thereby calculating the track irregularity values. However, in practical measurements, the impact of track irregularities and dynamic

variations in track geometry can induce multi-degree-of-freedom movements in the detection system. This motion may misalign the accelerometer's sensitive axis with the inertial reference, introducing measurement errors. Therefore, it is essential to remove interference components from the accelerometer signals [26]. The response of the vertical accelerometer can be expressed as follows:

$$\begin{cases} \alpha_{\mathrm{L}} = \frac{d^2 z_{\mathrm{L}}}{dt^2} + \mathrm{g}\cos\theta_{\mathrm{b}}\cos\psi_{\mathrm{b}} + \frac{1}{2}\mathrm{G}\frac{d^2\theta_{\mathrm{b}}}{dt^2} + v\omega_{\mathrm{z}}P \\ \alpha_{\mathrm{R}} = \frac{d^2 z_{\mathrm{R}}}{dt^2} + \mathrm{g}\cos\theta_{\mathrm{b}}\cos\psi_{\mathrm{b}} - \frac{1}{2}\mathrm{G}\frac{d^2\theta_{\mathrm{b}}}{dt^2} + v\omega_{\mathrm{z}}P \\ P = \cos\theta_{\mathrm{b}}\sin\psi_{\mathrm{b}}\sin\varphi_{\mathrm{b}} - \sin\theta_{\mathrm{b}}\cos\varphi_{\mathrm{b}} \end{cases} \tag{2}$$

where α_{L} and α_{R} represent the vertical acceleration measurements on the left and right sides, respectively; G is the horizontal distance between the left and right vertical accelerometers; θ_{b}, ψ_{b} and φ_{b} denote the roll, pitch, and yaw angles of the detection beam; z_{L} and z_{R} are the absolute displacements of the left and right vertical accelerometers in inertial space; g is the gravitational acceleration; and ω_z represents the yaw angular velocity of the detection beam.

The integrated displacement results, along with the measurements from the distance sensors, are mapped onto the corresponding track cross-section to obtain the left and right vertical irregularities, Z_{L} and Z_{R}. The vertical irregularities calculated using Equation (3) are widely applied in track inspection systems, referred to in this study as the acceleration integration method. Where θ_{s} represents the roll angle of the detection beam relative to the track plane; δ_{L} and δ_{R} denote the vertical relative displacements between the left and right vertical accelerometers and their respective rails.

$$\begin{cases} \theta_{\mathrm{s}} = \frac{\delta_{\mathrm{L}} - \delta_{\mathrm{R}}}{1500} \\ Z_{\mathrm{L}} = (z_{\mathrm{L}} + \delta_{\mathrm{L}})\cos\theta_{\mathrm{s}}\cos\psi_{\mathrm{b}} \\ Z_{\mathrm{R}} = (z_{\mathrm{R}} + \delta_{\mathrm{R}})\cos\theta_{\mathrm{s}}\cos\psi_{\mathrm{b}} \end{cases} \tag{3}$$

2.4. Validation of the Virtual Track Inspection Method

To validate the accuracy of the virtual track inspection technology based on the acceleration integration method, excitation irregularities were introduced into the track, enabling the train to operate under vertical excitation. The virtual vertical irregularities computed by the software were then compared with the excitation irregularities in both the time and frequency domains. For a time-domain comparison, a 2.5 m step-size sliding window was used to calculate the standard deviation of the error between the virtual and excitation irregularities, capturing amplitude variation information. For a frequency-domain comparison, Welch's power spectral density (PSD) estimation method [27] was employed to calculate the power spectral density of the data sequences, providing an insight into wavelength components.

The excitation irregularities adopted in this study were generated from the spectrum inversion of ballastless tracks on Chinese high-speed railways. It is described by a piecewise fitting approach using power functions, with each segment of the track spectrum represented by a unified expression [28], as shown in Equation (4):

$$S(\phi) = \frac{A}{\phi^n} \tag{4}$$

where $S(\phi)$ represents the power spectral density function; ϕ denotes the spatial frequency of the track irregularity, A and n are fitting coefficients, which can be obtained from Reference [29].

The excitation irregularities applied in the simulation model can be converted from spatial spectra into spatial irregularity sample sequences through numerical simulation methods. Given the focus on detection accuracy for long-wavelength vertical irregularities, the wavelength range of the excitation irregularities was set to 1–100 m, with a spatial sampling interval of 0.25 m. Simulations were conducted to obtain virtual vertical irregularities

at different inspection speeds of 80, 120, and 160 km/h. Figure 2 presents a comparison of the virtual and excitation irregularities at an inspection speed of 80 km/h.

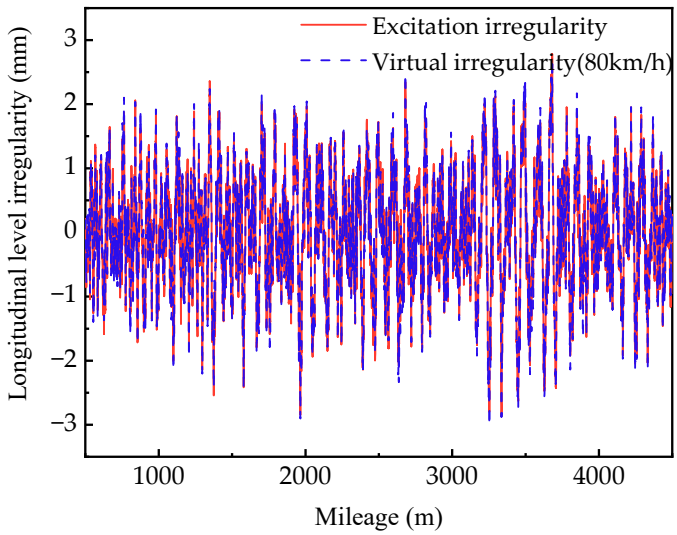

Figure 2. Comparison of virtual and incentive irregularity waveforms.

As shown in Figure 3a, although the calculation of virtual irregularities involves various interferences, including the train dynamics model, double integration, and high-pass filtering, the standard deviation of the error between the virtual and excitation irregularities remains generally within 0.05 mm. This indicates that the error is within an acceptable range.

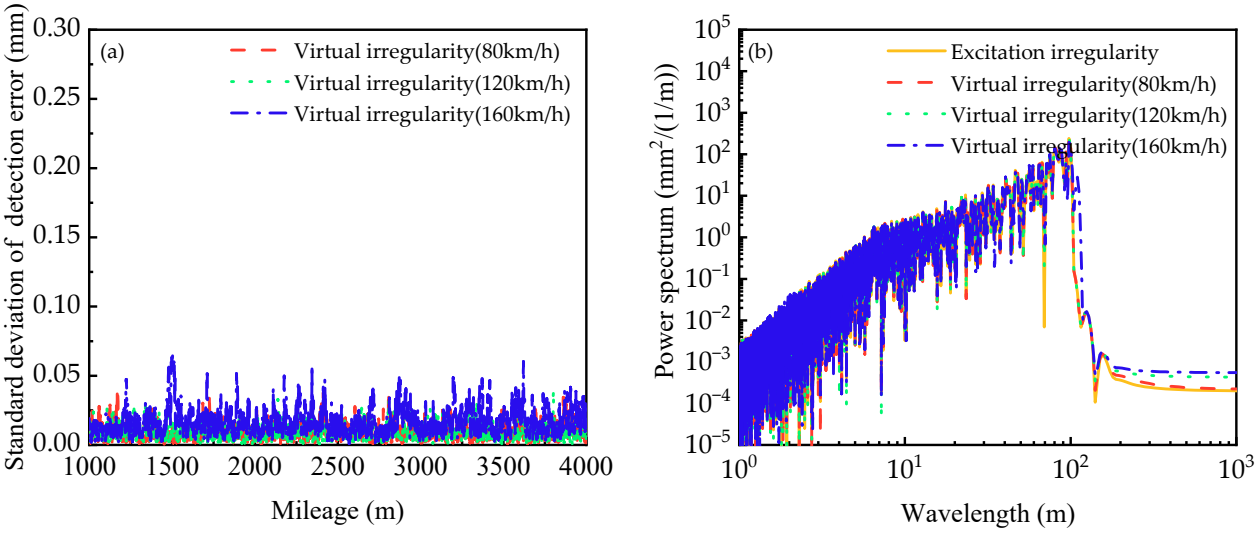

Figure 3. Comparison of time and frequency domain indexes of virtual and incentive irregularities at different speeds (**a**) Error standard deviation comparison (**b**) Power spectral density comparison.

Figure 3b demonstrates that the PSD curves of the virtual and excitation irregularities are largely consistent in both amplitude and trend, indicating that the wavelength components of the virtual irregularities obtained through the acceleration integration method align with those of the excitation irregularities across different detection speeds. Therefore, the virtual irregularities calculated via the acceleration integration method accurately reflect the amplitude and wavelength composition of the excitation irregularities, thereby validating the effectiveness of this approach.

3. Investigation of the Relationship Between Vertical Curves and Track Irregularities

With the accuracy of the proposed model and method validated, these tools were employed to analyze the factors influencing detection accuracy for tracking vertical irregularities in vertical curve segments. By varying key parameters—including train speed V, vertical curve length L, gradient i, gradient difference Δi, and radius R—we obtained virtual irregularities through the virtual track inspection method based on the acceleration integration approach. The virtual irregularities under different conditions were then compared with the excitation irregularities in both the time and frequency domains, identifying the primary factors affecting detection accuracy in vertical curve segments.

3.1. Impact of Train Operating Speed on Detection Accuracy

This section examines the impact mechanism of train operating speed on detection accuracy. Considering that the operating speed of most urban rail transit systems does not exceed 160 km/h, the test conditions were configured accordingly, as detailed in Table 1.

Table 1. Experimental conditions for speed variation.

Operating Conditions	Train Speed V (km·h^{-1})	Radius R (m)	Length L (m)	Gradient Difference Δi (‰)	Single-Side Gradient i (‰)
1	80	10,000	400	40	±20
2	120				
3	160				

After obtaining virtual dynamic responses under varying speed conditions, virtual irregularities were computed. Given the extensive track length, a 500 m segment in both directions from the centre of the vertical curve was selected to include the complete vertical curve and allow the precise analysis of errors between virtual and excitation irregularities. This segment was analyzed in both the time and frequency domains. In Figure 4a, the mileage ranges 1600–1900 m and 2300–2600 m represent straight gradient sections, while 1900–2300 m corresponds to the vertical curve segment.

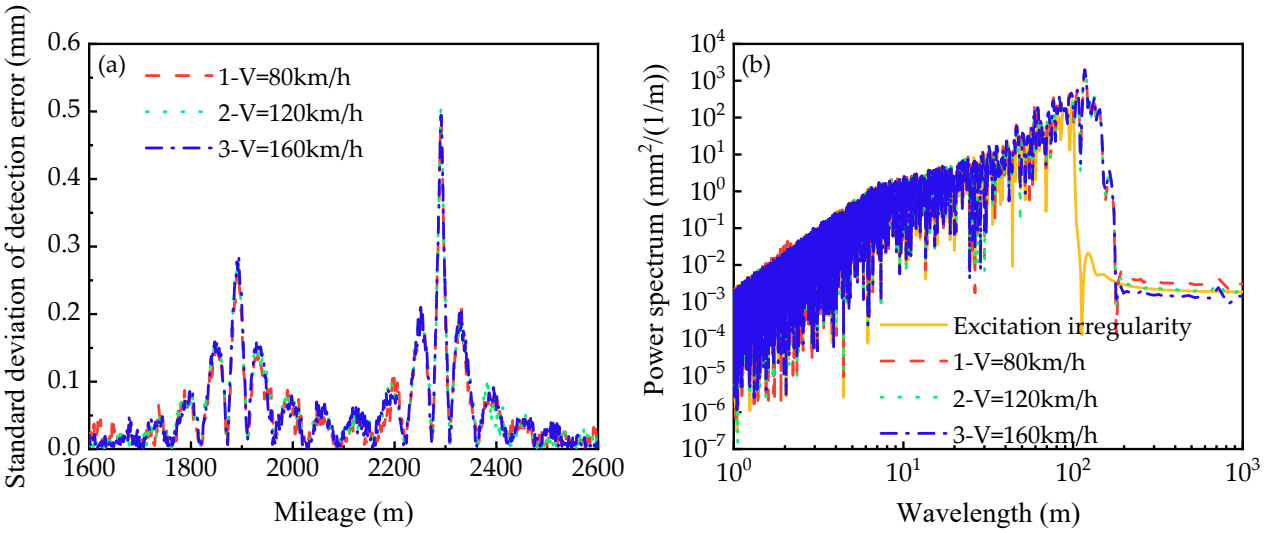

Figure 4. Time–frequency domain comparison of virtual and excitation irregularity metrics at different detection speeds (**a**) Comparison of error standard deviation (**b**) Comparison of power spectral density.

Figure 4a demonstrates that the virtual irregularities align well with the excitation irregularities across straight gradient sections and the central part of the vertical curve,

with the error standard deviation remaining within 0.1 mm. However, notable spikes occur near the transition points—tangent-to-curve and curve-to-tangent points—of the vertical curve. The spike amplitude begins to increase approximately 100 m before the transition point, reaching a peak at the transition point itself, and then gradually decreasing within 100 m beyond it. Additionally, the spike amplitude is more pronounced at the curve-to-tangent transition point. With increasing speed, the error standard deviation shows minimal variation, indicating that train speed has a limited effect on the amplitude accuracy of virtual irregularity detection at vertical curves, consistent with previous findings in the literature [18].

Figure 4b illustrates that within the wavelength range of 1–100 m, the PSD curves of the virtual and excitation irregularities exhibit strong alignment, with similar trends and amplitude. Speed variations have no significant effect on the overall shape of the PSD curve in this range. However, for wavelengths exceeding 100 m, the PSD values of the long-wavelength components in the virtual irregularities increase noticeably, with a slight rise in PSD values observed as the speed decreases.

3.2. Impact of Vertical Curve Gradient and Length on Detection Accuracy

The length, radius, and gradient of a vertical curve are interrelated, satisfying the relationship $L = R(\arctan i_1 - \arctan i_2)$. By controlling one factor, the effects of variations in the other factors on detection accuracy can be examined. In this section, the vertical curve radius is held constant while the gradient and length are varied to assess their impact on detection accuracy. According to relevant design standards, the maximum single-sided gradient for intercity railways should not exceed 30‰. The specific test conditions are outlined in Table 2.

Table 2. Experimental conditions for variations in vertical curve gradient and length.

Operating Conditions	Train Speed V (km·h^{-1})	Radius R (m)	Length L (m)	Gradient Difference Δi (‰)	Single-Side Gradient i (‰)
1	120	10,000	200	20	±10
2			400	40	±20
3			600	60	±30

After obtaining the virtual dynamic responses under varying conditions of vertical curve gradient and length, the virtual irregularities were computed. Similar to the previous section, a 500 m segment was extracted in both directions from the centre of the vertical curve to ensure full coverage of the curve for a time and frequency domain analysis. The results are shown in Figure 5.

Figure 5a shows that under varying vertical curve gradients and lengths, the standard deviation of error between the virtual and excitation irregularities remains largely consistent in magnitude, with variations in peak error locations attributable to changes in vertical curve length. Specifically, the error standard deviation stabilizes around 0.3 mm near the tangent-to-curve transition and 0.5 mm near the curve-to-tangent transition, indicating higher detection error near the latter. This suggests that gradient variations have minimal impact on the detection accuracy of virtual irregularities. Figure 5b demonstrates that the PSD curves of the virtual irregularities remain largely unchanged across different gradient and length conditions, with only noticeable differences from the excitation irregularities in the 100–120 m wavelength range. This discrepancy arises from the spatial cutoff frequency of the high-pass filter at 120 m, which does not fully eliminate the influence of the track alignment. In summary, gradient variations in the vertical curve have no significant impact on the wavelength components of the virtual irregularities, which aligns with the findings in [19].

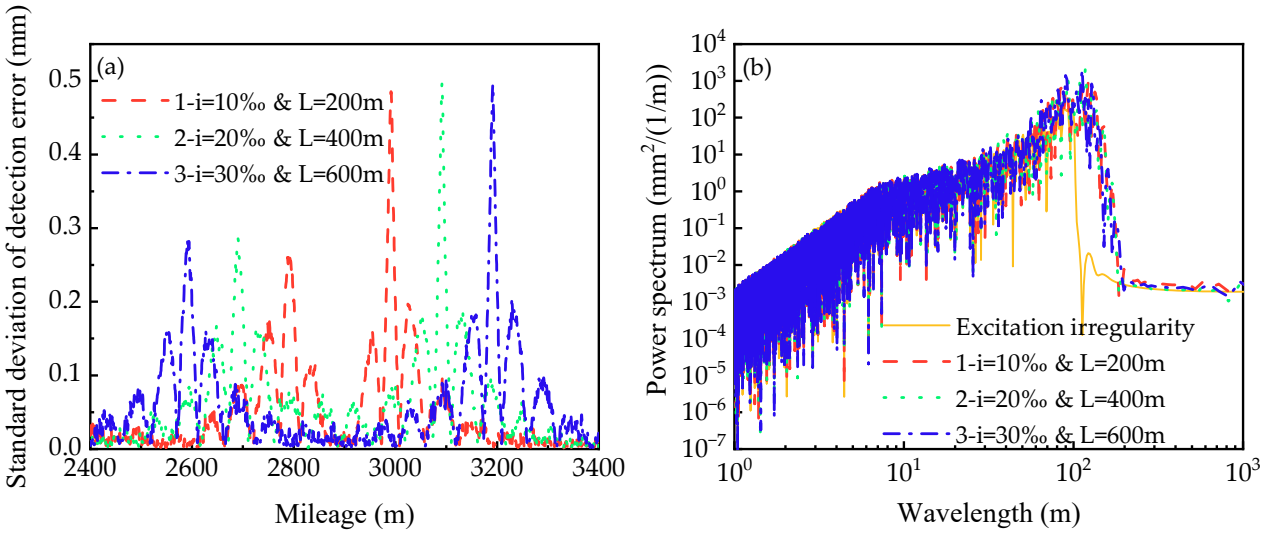

Figure 5. Time–frequency domain comparison of virtual and excitation irregularity metrics under varying vertical curve gradients and lengths (**a**) Comparison of error standard deviation (**b**) Comparison of power spectral density.

3.3. Impact of Vertical Curve Gradient and Radius on Detection Accuracy

In this section, the vertical curve length remains constant while the radius and gradient are varied to investigate their impact on detection accuracy. Based on Equation (1) and the selected a_{sh} values, calculations were performed, and the vertical curve radius was rounded to obtain a range of 6000–14,000 m. The specific test conditions are detailed in Table 3.

Table 3. Experimental conditions for variations in vertical curve gradient and radius.

Operating Conditions	Train Speed V (km·h^{-1})	Radius R (m)	Length L (m)	Gradient Difference Δi (‰)	Single-Side Gradient i (‰)
1	120	6000	400	66.66	±33.33
2		10,000		40	±20
3		14,000		28.58	±14.29

After obtaining the virtual dynamic responses under varying vertical curve gradient and radius conditions, virtual irregularities were computed. Similar to the previous section, a 500 m segment was extracted from the vertical curve centre for a time–frequency domain analysis in both directions. The results are shown in Figure 6. As demonstrated in the previous section, the effect of vertical curve gradient on the error standard deviation and irregularity wavelength components is negligible.

Figure 6a shows that the vertical curve radius is a critical factor influencing the detection accuracy of vertical irregularities in curve segments; smaller radii result in larger error standard deviations. The location of peak detection errors is determined solely by the vertical curve length. Figure 6b indicates that changes in vertical curve gradient and radius do not affect the overall trend of the PSD curve of the virtual irregularities, with only limited impact on PSD amplitude.

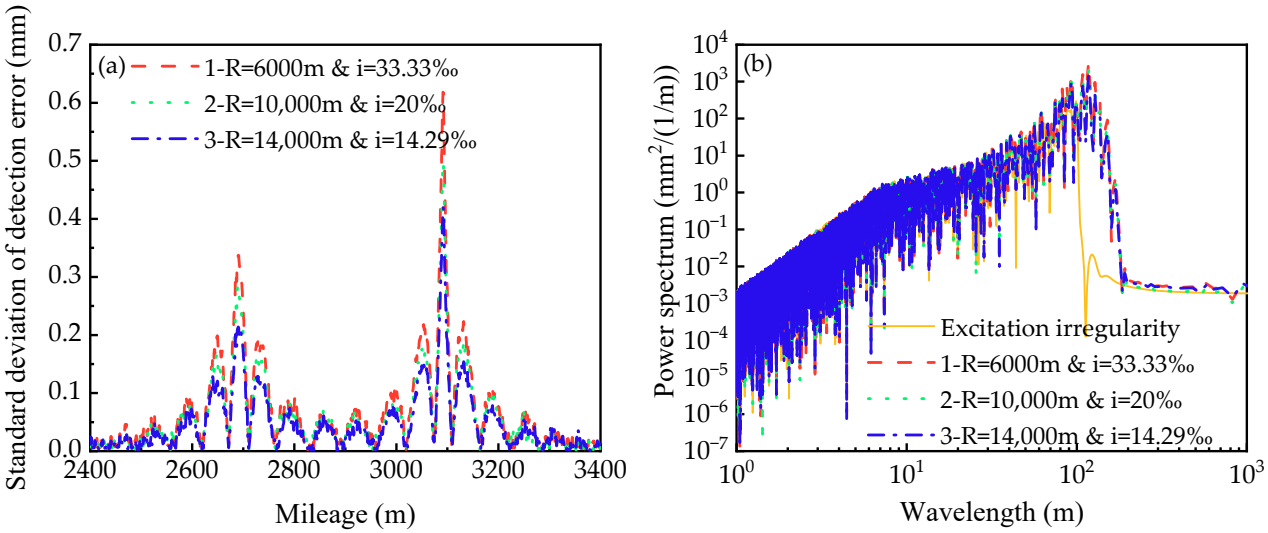

Figure 6. Time–frequency domain comparison of virtual and excitation irregularity metrics under varying vertical curve gradients and radii (**a**) Comparison of error standard deviation (**b**) Comparison of power spectral density.

3.4. Impact of Vertical Curve Radius and Length on Detection Accuracy

In this section, the vertical curve gradient remains constant while the radius and length are varied to examine their effects on detection accuracy. The radius values are consistent with those in the previous section, and the specific test conditions are outlined in Table 4.

Table 4. Experimental conditions for variations in vertical radius and length.

Operating Conditions	Train Speed V (km·h^{-1})	Radius R (m)	Length L (m)	Gradient Difference Δi (‰)	Single-Side Gradient i (‰)
1	120	6000	240	40	±20
2		10,000	400		
3		14,000	560		

After obtaining virtual dynamic responses under varying vertical curve radius and length conditions, virtual irregularities were computed. As in the previous section, a 500 m segment in both directions from the curve centre was selected for the time–frequency domain analysis, as shown in Figure 7.

In conjunction with the findings from Sections 3.1–3.3 and Figure 7, it is further confirmed that the vertical curve radius is the primary factor affecting detection accuracy for vertical irregularities in the longitudinal profile. While the radius does not impact the wavelength composition of the virtual irregularities, it has a subtle effect on the power spectral density amplitude. Additionally, the location of peak detection errors is determined solely by the vertical curve length.

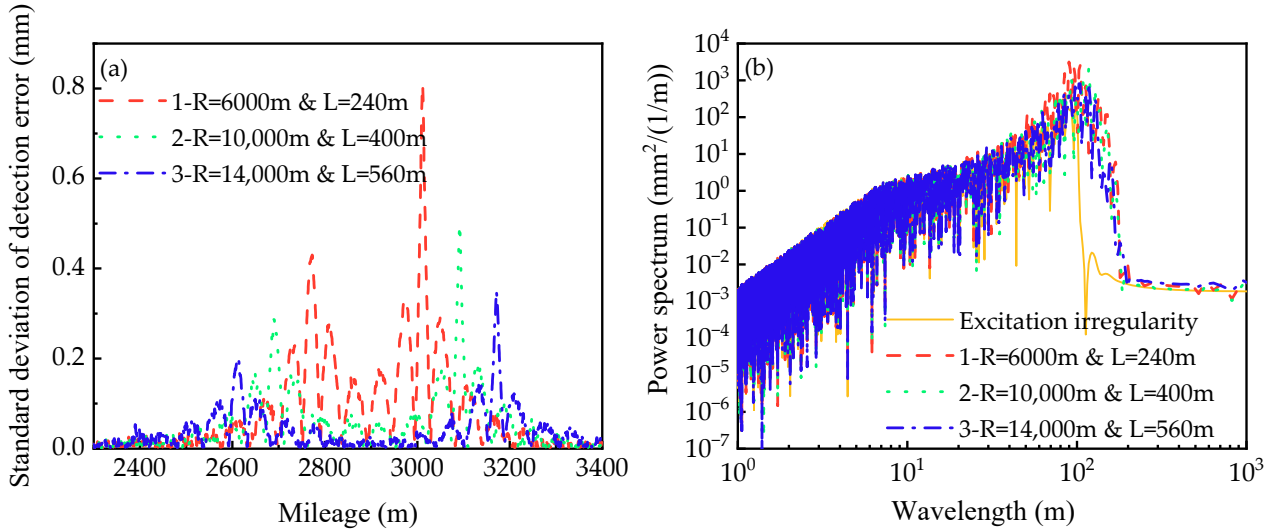

Figure 7. Time–frequency domain comparison of virtual and excitation irregularity metrics under varying vertical curve radii and lengths (**a**) Comparison of error standard deviation (**b**) Comparison of power spectral density.

4. Optimization of Detection Algorithms for Vertical Curve Segments

4.1. Analysis of Factors Affecting Detection Accuracy Due to Vertical Curves

A segment of simulation data from a specific condition in Section 3 was selected for spectral analysis, as shown in Figure 8. Figure 8 indicates that, in the time domain, significant differences appear between the high-pass filtered virtual irregularities and excitation irregularities near the tangent-to-curve and curve-to-tangent transition points. In the frequency domain, notable discrepancies occur in the low-frequency range. This is attributed to the high-pass filter's cutoff frequency of 120 m, which does not fully eliminate the low-frequency components—specifically, the track alignment—in the acceleration integration results.

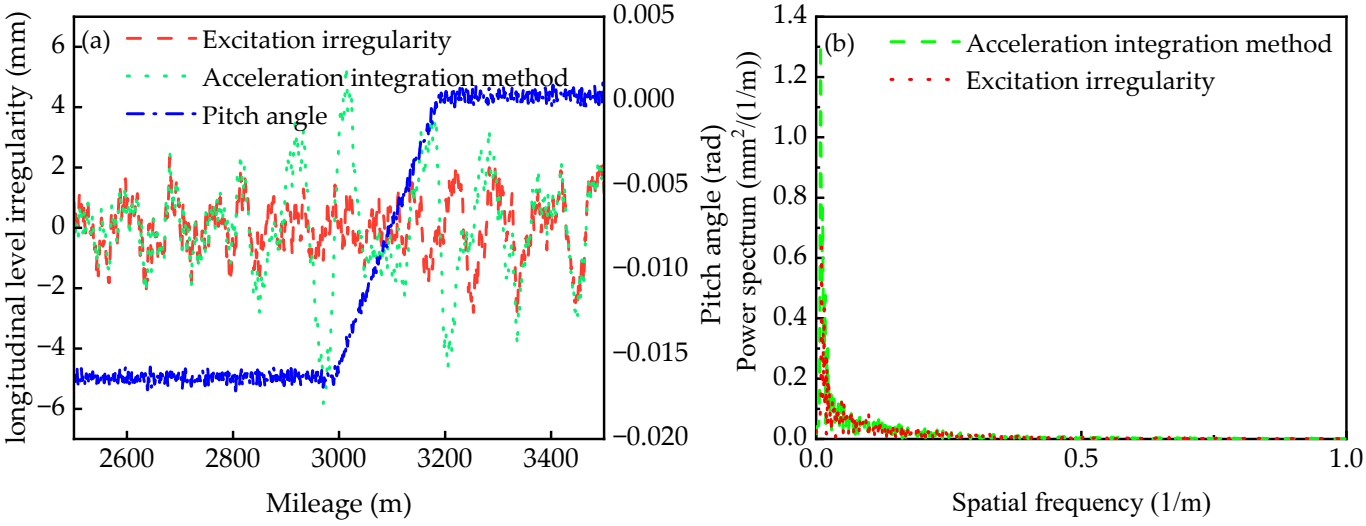

Figure 8. Error analysis of the acceleration integral method (**a**) Track irregularity comparison (**b**) Detection result amplitude-spatial frequency spectrum.

The above analysis demonstrates that the longitudinal profile alignment significantly impacts the accuracy of track dynamic irregularity detection, resulting in increased detection errors near gradient transition points and occasionally triggering abnormal exceedances in practical inspections. This is due to the spatial frequency of track alignment

changes near transition points being close to the 100–120 m long-wavelength irregularity frequency. Variations in train speed and vertical curve radius further shift the low-frequency components induced by track alignment in the frequency domain, making it challenging to set an appropriate spatial cutoff frequency that preserves relevant track irregularity data while effectively eliminating low-frequency interference from track alignment. Consequently, relying solely on high-pass filtering presents inherent limitations.

4.2. Reference Cancellation Method

The acceleration integration method establishes a unified inertial reference framework to calculate track irregularities, reflecting the characteristics of track alignment variations within inertial space. As indicated by the above analysis, this reference framework impacts the detection accuracy of long-wavelength vertical irregularities in vertical curve segments along the longitudinal profile. To address this, we propose a reference cancellation method that removes track alignment components from the acceleration integration results, preserving only the track irregularity information. High-pass filtering is then applied to enhance the detection accuracy of long-wavelength vertical irregularities in vertical curve segments.

The pitch angle ψ_{b} of the detection beam is largely insensitive to variations in horizontal track alignment but is highly sensitive to changes in vertical alignment, enabling precise reflection of gradient variations in the longitudinal profile within inertial space. By applying line integration principles, spatial integration of ψ_{b} yields the spatial measurement curve Z_{m} of the track's longitudinal profile, calculated as follows:

$$Z_{\mathrm{m}} = \int \psi_{\mathrm{b}} ds \tag{5}$$

The relationship between the pitch angle of the detection beam ψ_{b}, and the true spatial curve of the track's longitudinal profile Z_{t}, is given by:

$$\psi_{\mathrm{b}}(x) = \frac{Z_{\mathrm{t}}(x) - Z_{\mathrm{t}}(x - \mathrm{L})}{\mathrm{L}} \tag{6}$$

where L represents the wheelbase of the bogie.

Applying the Laplace transform to Equation (6) and substituting the transformed result of Equation (5) yields the transfer function $H(s)$ relating the spatial measurement curve Z_{m} to the true spatial curve Z_{t}.

$$H(s) = \frac{1 - e^{-s\mathrm{L}}}{s\mathrm{L}} \tag{7}$$

where $s = j2\pi/\lambda$, with λ representing the wavelength.

The amplitude–frequency characteristic curve of the testing system illustrates the relationship between the measured values and the true values. The amplitude–frequency characteristic curve corresponding to the transfer function $H(s)$ is shown in Figure 9. Figure 9 indicates that the virtual irregularities derived from the transfer function $H(s)$ exhibit significant attenuation of high-frequency disturbances, effectively serving as a low-pass filter for the true spatial curve Z_{t}. In the acceleration integration method, the theoretical approach directly calculates track irregularities through acceleration integration, yielding a transfer function of 1. Consequently, by taking the difference between the results of the second integration of acceleration and the integration of the pitch angle $\hat{\psi}_b$, it is possible to eliminate the track alignment components contained in the acceleration integration results while retaining only the track irregularity data. The resulting vertical irregularities calculated using this method are referred to as the reference cancellation method in this study.

$$\begin{cases} Z_{\mathrm{L}} = (z_{\mathrm{L}} - Z_{\mathrm{m}} + \delta_{\mathrm{L}}) \cos\theta_{\mathrm{s}} \cos\psi_{\mathrm{b}} \\ Z_{\mathrm{R}} = (z_{\mathrm{R}} - Z_{\mathrm{m}} + \delta_{\mathrm{R}}) \cos\theta_{\mathrm{s}} \cos\psi_{\mathrm{b}} \end{cases} \tag{8}$$

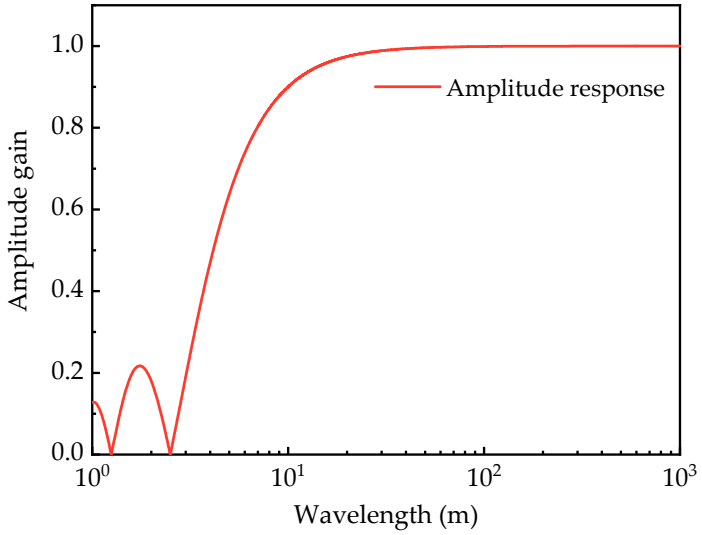

Figure 9. Amplitude–frequency characteristics of H (s).

The core of the reference cancellation method lies in obtaining an ideal pitch angle dataset that accurately represents the track alignment, thereby minimizing its impact on detection accuracy. The spatial curve of the ideal pitch angle is a horizontal line on level and straight gradient sections, and a line with a constant, non-zero slope in vertical curve segments. The measured pitch angle comprises a low-frequency component induced by the track alignment (the ideal pitch angle) and high-frequency disturbances caused by track irregularities. To eliminate high-frequency interference from track irregularities, a low-frequency-response inclinometer is employed to measure the pitch angle of the detection beam. The measured results are processed using mean filtering, which approximates the filtered output $\hat{\psi}_b$ as the angle between the track and the ground reference line. The mean filtering process can be represented as follows:

$$\hat{\psi}_b(i) = \frac{1}{2N+1}(\psi_b(i-N) + \cdots + \psi_b(i+N)) \tag{9}$$

Figure 10 presents a comparison of the spatial curves for the actual and ideal pitch angles, where the difference lies in the presence or absence of track irregularities. In the figure, the sections from 1000–1200 m, 1900–2300 m, and 3000–3200 m represent vertical curves, while 1200–1900 m and 2300–3000 m are straight gradient segments, with the remaining sections being level track. After smoothing, the actual pitch angle closely approximates the ideal pitch angle, providing an intuitive representation of the track's alignment in the longitudinal profile.

Although the smoothed results exhibit a high degree of smoothness, some undulations caused by long-wavelength irregularities remain, creating minor deviations from the ideal pitch angle spatial curve. To achieve a close approximation of the smoothed pitch angle to the ideal pitch angle and further reduce the impact of track irregularities on the reference cancellation method, a piecewise linear fitting approach is employed for the smoothed pitch angle. This method substitutes the smoothed pitch angle with linear segments, enhancing algorithm precision. The core of this approach lies in accurately identifying segmentation points that reflect changes in track alignment, allowing linear segments to replace the smoothed curves.

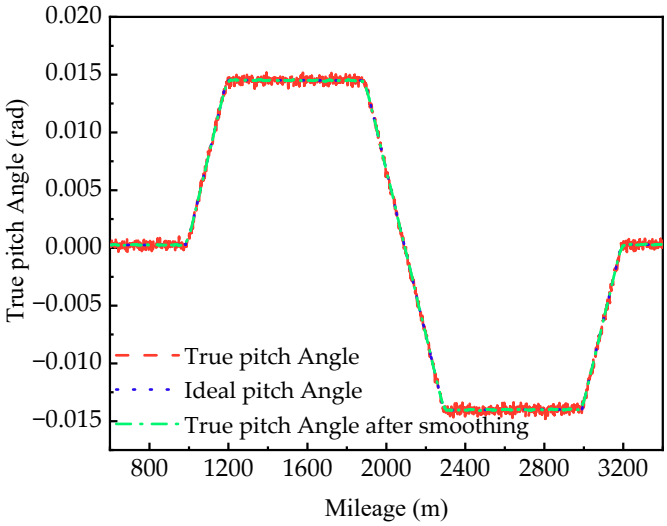

Figure 10. Comparison of detection beam pitch angle over mileage.

Figure 10 indicates that the longitudinal profile alignment changes significantly at segmentation points. Therefore, a threshold is established. A segment of data approximately 50 m in length is then selected for linear fitting, starting from a horizontal line. Subsequently, the distances from new data points to the fitted line are iteratively calculated. If three consecutive new data points exceed the specified threshold distance from the line, the second point is marked as a track alignment segmentation point. Upon completing the identification of all segmentation points, orthogonal least squares (OLS) linear fitting is performed for each segment to approximate the ideal pitch angle. It is important to note that the established threshold is related to the magnitude of the track gradient. The steps for the OLS linear fitting process are as follows [30]:

(1) Formulate the linear equation and solve for estimated line parameters. Given the line equation $y = ax + b$, calculate the estimated line equation $y = a_0x + b_0$ based on segmentation points $m_1(x_1, y_1)$ and $m_2(x_2, y_2)$.

$$\begin{cases} a = a_0 + \xi_a \\ b = b_0 + \xi_b \end{cases} \tag{10}$$

where a and b are the parameters to be determined; a_0 and b_0 are the approximate parameter values; ξ_a and ξ_b represent the correction values for the parameters.

(2) Derivation of Single-Point Linear Fitting Residual. Calculate the distance s_i from point $m_i(x_i, y_i)$ to the line $y = a_0x + b_0$, and perform a second-order Taylor expansion on s_i to obtain the single-point fitting residual.

$$s_i = \frac{a_0x_i - y_i + b_0 + \xi_b}{\sqrt{a_0^2 + 1}} + \frac{x_i + a_0y_i - a_0b_0}{(a_0^2 + 1)^{3/2}}\xi_a \tag{11}$$

(3) Substitute multiple points into Equation (11) to obtain the linear fitting residual equation and solve for the unknown parameters.

$$S = A\xi - B \tag{12}$$

$$\xi = (A^TA)^{-1}(A^TB) \tag{13}$$

where $S = \begin{pmatrix} s_1 \\ \cdots \\ s_n \end{pmatrix}, \xi = \begin{pmatrix} \xi_a \\ \xi_b \end{pmatrix}, A = \begin{pmatrix} \frac{x_1 + a_0y_1 - a_0b_0}{(a_0^2+1)^{3/2}}, \frac{1}{\sqrt{a_0^2+1}} \\ \cdots \\ \frac{x_n + a_0y_n - a_0b_0}{(a_0^2+1)^{3/2}}, \frac{1}{\sqrt{a_0^2+1}} \end{pmatrix}, S = \begin{pmatrix} \frac{y_1 - a_0x_1 - b_0}{\sqrt{a_0^2+1}} \\ \cdots \\ \frac{y_n - a_0x_n - b_0}{\sqrt{a_0^2+1}} \end{pmatrix}.$

The algorithm flow is shown in Figure 11.

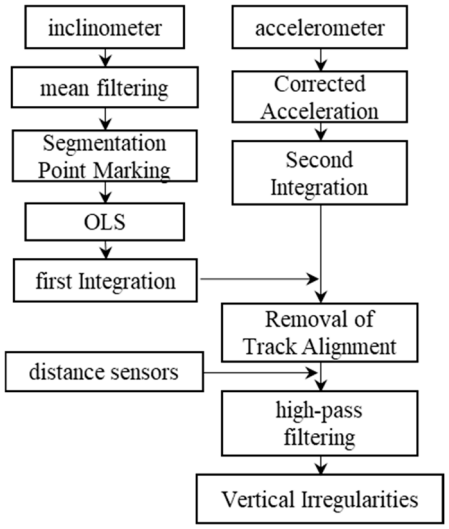

Figure 11. Flowchart of the reference cancellation method.

A segment of simulation data from a specific condition in Section 3 was selected for acceleration integration and pitch angle integration, with the selected pitch angle data undergoing mean smoothing filtering and orthogonal least-squares fitting. The calculation results are shown in Figure 12. As observed in Figure 12a, both the acceleration integration and pitch angle integration results capture the height variation in the track profile in the vertical alignment space. The acceleration integration result additionally includes the vertical oscillations induced by track irregularities. Figure 12b presents the difference between the two results; a minor trend component remains due to deviations between the identified and actual track segmentation points. Nevertheless, the overall track profile shape has been largely removed, and applying a high-pass filter at this stage would significantly improve detection accuracy.

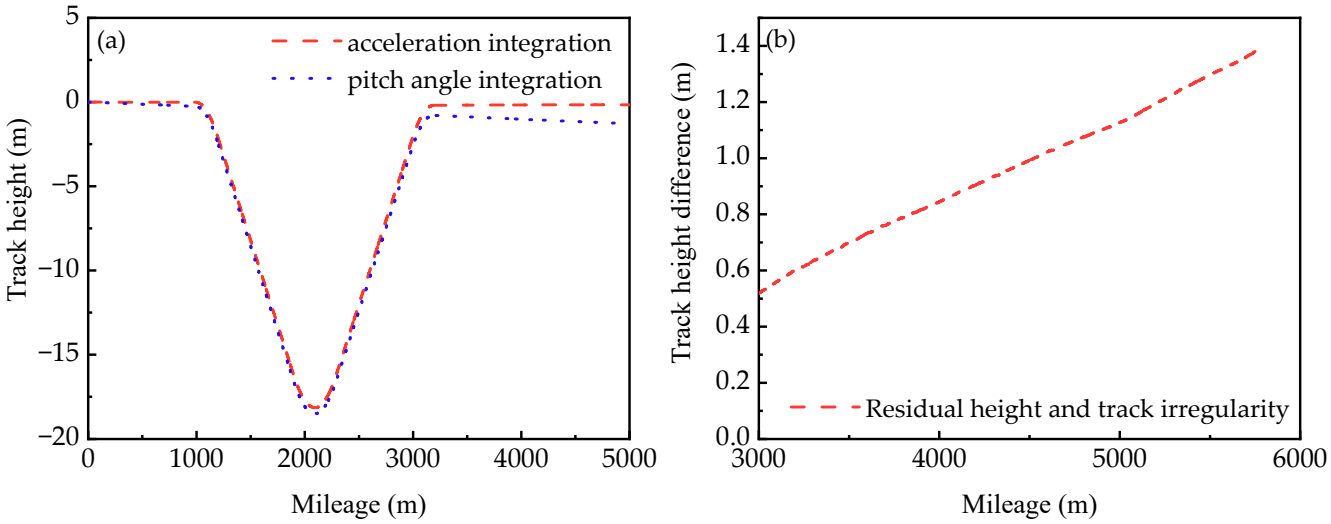

Figure 12. Time domain comparison of acceleration integration and pitch angle integration results (**a**) Time domain comparison of integration results, (**b**) Time domain comparison of integration result differences.

4.3. Algorithm Verification

Simulation analyses were conducted under various test conditions, and the results were compared with those obtained using the acceleration integration method to validate

the effectiveness of the reference cancellation method. The parameter values for each test are consistent with those described previously, as detailed in Table 5.

Table 5. Experimental conditions under different algorithms.

Operating Conditions	Train Speed V (km·h^{-1})	Radius R (m)	Length L (m)	Gradient Difference Δi (‰)	Single-Side Gradient i (‰)
1	120	10,000	400	40	±20
2	80	10,000	400	40	±20
3	120	10,000	600	60	±30
4	120	14,000	400	28.58	±14.59
5	120	14,000	560	40	±20

After simulating the virtual dynamic responses, virtual irregularities were calculated. The maximum error E_{max} and root mean square error E_{rmse} for both algorithms under different test conditions were then statistically analyzed, as shown in Table 6. The results from Scenario 4 were selected for visualization. Following the methodology outlined in Section 3, a 500 m segment was extracted in both directions from the centre of the vertical curve for time–frequency domain analysis, as illustrated in Figure 13.

Table 6. Experimental results under different algorithms.

Conditions / Method	1		2		3		4		5	
	E_{max}	E_{rmse}	E_{max}	E_{rmse}	E_{max}	E_{rmse}	E_{max}	E_{rmse}	E_{max}	E_{rmse}
Acceleration integration	5.03	1.12	5.33	1.13	5.02	1.17	3.73	0.82	3.69	0.86
reference cancellation	1.42	0.15	1.54	0.23	1.44	0.16	1.85	0.17	1.36	0.14

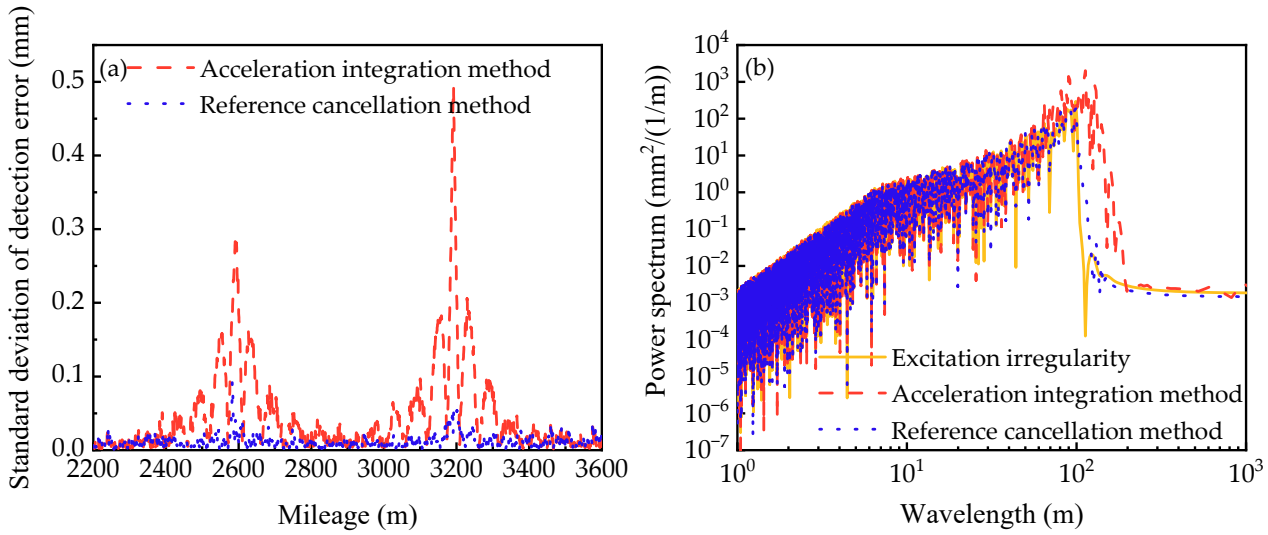

Figure 13. Time–frequency domain comparison of different algorithms (**a**) Comparison of error standard deviation (**b**) Comparison of power spectral density.

Figure 13a shows that in straight and gradient sections, the detection accuracy of the reference cancellation method is comparable to that of the acceleration integration method, with no significant difference in error. However, in vertical curve segments, the reference cancellation method markedly reduces detection errors, achieving a higher level of accuracy. This method effectively lowers the detection error in vertical curve segments to levels similar to those in straight sections. At the transition points at 2600 m and 3200 m, minor error spikes remain, likely due to residual discrepancies in the pitch angle processing despite the use of smoothing filters and orthogonal least squares fitting to approximate ideal

conditions. Overall, the reference cancellation method shows substantial improvement in detection accuracy for vertical curve segments.

Figure 13b demonstrates that the reference cancellation method maintains the amplitude and trend of the short-wavelength components in the PSD curve of virtual irregularities. For wavelengths greater than 100 m, the PSD curve derived from the reference cancellation method aligns more closely in amplitude and trend with the reference irregularity curve, effectively mitigating the influence of track alignment on the PSD of long-wavelength irregularities.

Table 6 shows that under different test conditions, the maximum detection error E_{max} and the root mean square E_{rmse} of the acceleration integration method exhibit significant variation. This discrepancy primarily arises from the use of a uniform high-pass filter, while differences in spatial frequency across varying vertical curve radii result in inconsistent filtering effects. Compared to the acceleration integration method, the reference cancellation method effectively removes the track alignment component from the acceleration integration results before high-pass filtering, significantly enhancing the accuracy of virtual irregularity detection. This method achieves comparable detection accuracy to the acceleration integration method on straight and level sections while demonstrating substantially higher accuracy on vertical curve sections, with maximum detection error E_{max} and root mean square E_{rmse} reduced by 71.77% and 86.61%, respectively.

In summary, a key limitation of the acceleration integration method lies in the inability of the high-pass filter to completely remove low-frequency components introduced by vertical curves. In contrast, the advantage of the reference cancellation method is that it does not require the design of different spatial cutoff frequencies for various track alignments; it achieves consistent detection accuracy using a single high-pass filter cutoff frequency. However, this method also has a notable drawback: if ideal pitch angle data cannot be obtained, the detection accuracy may be compromised.

5. Conclusions

This study addresses the issue of significant long-wavelength irregularity detection errors during dynamic measurements of track vertical irregularities, which arise due to the spatial frequency characteristics of vertical curve segments being similar to those of certain long-wavelength irregularities. A comprehensive vehicle-track multibody dynamics simulation model was established to tackle this issue, and the model's validity was verified by applying excitation irregularities. Subsequently, the effects of variations in train speed and key vertical curve design parameters on irregularity detection errors were investigated. The reference cancellation method was proposed by analyzing the mechanisms behind the elevated detection errors in vertical curve segments to enhance the accuracy of vertical irregularity detection. Various experimental conditions were designed to compare virtual irregularities calculated using the reference cancellation method and the inertial reference method, thereby validating the effectiveness of the proposed approach. This research provides a theoretical basis for improving track irregularity detection accuracy and facilitating track maintenance operations. Notably, the core of the reference phase cancellation method lies in obtaining ideal pitch angle data. In practical applications, an inclinometer sensor with a low-frequency response range should be selected to measure the pitch angle of the detection system. Additionally, it is essential to ensure that the inclinometer's sensitive axis is aligned parallel to the direction of track movement to minimize detection errors caused by the rolling and yawing motions of the detection device.

The main conclusions are as follows:

(1) Simulation analyses reveal that detection errors for track vertical irregularities significantly increase when trains pass through vertical curve segments, particularly at gradient transition points and their vicinity. The degree of impact from different vertical curve design parameters on detection accuracy varies. The detection errors at gradient transition points are primarily influenced by the vertical curve radius; smaller radii correlate with larger detection errors. The vertical curve length is the sole

factor determining the location of peak detection errors, which begin to increase 100 m before the transition point, reach their maximum at the transition point, and decrease to levels comparable to those in straight sections within 100 m after the transition.

(2) The proposed reference cancellation method effectively removes track alignment components from the acceleration integration results. This method achieves a detection accuracy comparable to the acceleration integration method in straight and gradient sections, while significantly enhancing the accuracy in vertical curve segments. By employing the reference cancellation method, detection errors in vertical curve segments can be reduced to levels equivalent to those in straight and gradient sections, and it does not alter the power spectral density of track irregularities.

(3) Various experimental conditions were established to validate the effectiveness of the reference cancellation method compared to the acceleration integration method under different scenarios. Simulation results indicate that, in comparison to the acceleration integration method, the reference cancellation method can reduce the maximum detection error $E_{\max}$ and the root mean square error E_{rmse} by up to 71.77% and 86.61%, respectively.

Author Contributions: Conceptualization, C.C.; methodology, C.C. and R.X.; software, R.X.; validation, R.X.; formal analysis, C.C. and R.X.; resources, C.C.; writing—original draft preparation, C.C. and R.X.; writing—review and editing, C.C.; supervision, C.C. All authors have read and agreed to the published version of the manuscript.

Funding: This research was funded by the National Natural Science Foundation of China (No. 52372402) and the National Natural Science Foundation of China (U2034210).

Institutional Review Board Statement: Not applicable.

Informed Consent Statement: Not applicable.

Data Availability Statement: The original contributions presented in the study are included in the article, further inquiries can be directed to the corresponding author.

Conflicts of Interest: The authors declare no conflicts of interest.

References

1. Wang, Y.; Chen, S.; Wei, S.; Yu, l.; Yang, F.; Fei, J. Study on Dynamic Measurement Method and Application of Rail Surface Slope and Vertical Curve Radius for High Speed Railways. *J. China Railw. Soc.* **2024**, *46*, 176–183. [CrossRef]
2. Li, Q.; Dai, B.; Yang, F.; Shi, L.; Wu, Y. Overview on Existing and Developing Methods for Track Irregularity Detection. *J. China Railw. Soc.* **2024**, *46*, 101–116. [CrossRef]
3. Niu, L.; Liu, J.; Qu, J.; Ying, F. Study of Relation between Track Irregularity and Lateral Acceleration of Vehicle Based on State-space Model. *J. China Railw. Soc.* **2020**, *42*, 123–129. [CrossRef]
4. Xu, P.; Liu, R.; Sun, Q.; Wang, F. A Novel Short-Range Prediction Model for Railway Track Irregularity. *Discret. Dyn. Nat. Soc.* **2012**, *2012*, 1951–1965. [CrossRef]
5. Li, Z.; Molodova, M.; Núñez, A.; Dollevoet, R. Improvements in Axle Box Acceleration Measurements for the Detection of Light Squats in Railway Infrastructure. *IEEE Trans. Ind. Electron.* **2015**, *62*, 4385–4397. [CrossRef]
6. Xin, T.; Wang, P.; Ding, Y. Effect of Long-Wavelength Track Irregularities on Vehicle Dynamic Responses. *Shock. Vib.* **2019**, *2019*, 4178065. [CrossRef]
7. Gao, Y.; You, M.; Yang, F.; Zhi, Y.; Zhang, Y.; Zhao, W.; Li, W. Study on the influence of subgrade settlement on car body vibration of high-speed railway. *J. Railw. Sci. Eng.* **2023**, *20*, 1139–1148. [CrossRef]
8. Wang, Q.; Zhao, H.; Gong, D.; Zhou, J.; Xiao, Z. Quantitative Detection of Vertical Track Irregularities under Non-Stationary Conditions with Variable Vehicle Speed. *Sensors* **2024**, *24*, 3804. [CrossRef]
9. Hung, C.F.; Hsu, W.L. Influence of long-wavelength track irregularities on the motion of a high-speed train. *Veh. Syst. Dyn.* **2017**, *56*, 95–112. [CrossRef]
10. Tan, S.; Shi, J.; Zhang, Y. Optimization of Vertical Curve Smoothness in High-speed Railway and Its Engineering Application. *J. Railw. Eng. Soc.* **2024**, *41*, 13–19. [CrossRef]
11. He, Q.; Xu, S.; Gao, T.; Hu, J.; Zhu, Y.; Wang, P. The Influence of Line Key Points on Vertical Parameters Design of 400 km/h High-speed Railway. *J. Railw. Eng. Soc.* **2022**, *39*, 25–32. [CrossRef]
12. Long, X.; Shi, J.; Fang, W. Evaluation of Ride Comfort Caused by Track Vertical Alignment of High-speed Railway. *J. Railw. Eng. Soc.* **2015**, *32*, 48–53. [CrossRef]

13. Wang, K.; Lv, K. Dynamic Evaluation Index System for Spatial Alignment of High-Speed Railway. *J. Southwest Jiaotong Univ.* **2016**, *51*, 227–235. [CrossRef]
14. Jiang, D.; Xie, Y.; Yi, S.; Lin, X.; Chen, W. Study on Vertical Curve Radius of Moscow-Kazan High-speed Railway. *Railw. Stand. Des.* **2018**, *62*, 24–29. [CrossRef]
15. Liu, Y. Determination of High Speed Railway Vertical Curve Parameters and Dynamic Analysis. *Railw. Eng.* **2019**, *59*, 125–128. [CrossRef]
16. Deng, J.; Sun, G.; Feng, Q. Research and Optimization on the Adaptability of 250km/h High Speed Railway Line Speed Increase. *Railw. Stand. Des.* **2024**, *68*, 1–6. [CrossRef]
17. Wang, Y. An Approach to 140 km/h Metro Line Technical Standard. *Railw. Stand. Des.* **2016**, *60*, 67–72. [CrossRef]
18. Wu, X. Research and analysis on the problem of vertical long wave irregularity in hang-chang high-speed railway. *Shanghai Railw. Sci. Technol.* **2015**, *3*, 8–9+19. [CrossRef]
19. Li, S.; Yi, Y.; Wang, Y.; Chen, Z.; Wang, P. Study on profile line regularity based on the inertial reference method in high-speed railway. *J. Railw. Sci. Eng.* **2018**, *15*, 1901–1910. [CrossRef]
20. Yang, F.; Sun, X.; Ning, Y.; Liu, B.; Tan, S.; Liang, C. The Influence of Vertical Curve on Track Dynamic Irregularity for High-speed Railway. *J. Railw. Eng. Soc.* **2023**, *40*, 16–22+61. [CrossRef]
21. Wu, Y. Research on Urban Rail Transit Line Technical Conditions. *Railw. Stand. Des.* **2018**, *62*, 39–44+49. [CrossRef]
22. *GB50157-2013*; Code for Design of Metro. China Building Industry Press: Beijing, China, 2014.
23. *TB 10624-2020*; Code for Design of Suburban Railway. China Railway Publishing House: Beijing, China, 2021.
24. *T/CAMET 01001-2019*; Technical Specification of Metropolitan Rapid Rail Transit. China Urban Rail Transit Association: Beijing, China, 2019.
25. Yu, J.; Gao, Y.; Wang, C.; Deng, G.; Su, Y.; Li, M. Detection and Early Warning System of Track High and Low Irregularity Based on Inertial Reference Method. *J. Transp. Eng.* **2021**, *21*, 33–39. [CrossRef]
26. Obrien, E.J.; Quirke, P.; Bowe, C.; Cantero, D. Determination of railway track longitudinal profile using measured inertial response of an in-service railway vehicle. *Struct. Health Monit.* **2018**, *17*, 1425–1440. [CrossRef]
27. Zhou, H.; Yao, B.; Ye, K.; Li, G.; Guo, j. Research on Underwater Noise Features Based on Spectrum Analysis and Welch Algorithm. *J. Internet Technol.* **2021**, *22*, 715–723. [CrossRef]
28. Zhou, Z.; Zhong, K.; Chen, L.; Li, X. Numerical Simulation of track stochastic irregularity and analysis of its effects on environmental vibration. *J. Basic Sci. Eng.* **2020**, *28*, 1410–1419. [CrossRef]
29. Kang, X.; Liu, X.; Li, H.; Yang, F.; Gao, J.; Zhan, W. PSD of ballastless track irregularities of high-speed railway. *Sci. Sin. Technol.* **2014**, *44*, 687–696. [CrossRef]
30. Shi, P. Orthogonal least square method is used to fit existing lines. *Sichuan Archit.* **2017**, *37*, 92–95. [CrossRef]